

Interplay between activity, elasticity, and liquid transport in self-contractile biopolymer gels

Anne Bernheim-Groswasser^{✉*} and Gefen Livne^{✉†}

Department of Chemical Engineering, Ben-Gurion University, Be'er Sheva 8774624, Israel

Paola Nardinocchi^{✉‡} and Filippo Recrosi^{✉§}

Department of Structural Engineering & Geotechnic, Sapienza Università di Roma, 00184 Roma, Italy

Luciano Teresi^{✉||}

Department of Mathematics & Physics, Università Roma Tre, 00146 Roma, Italy



(Received 14 August 2023; accepted 29 November 2023; published xxxxxxxxxx)

Active gels play an important role in biology and in inspiring biomimetic active materials, due to their ability to change shape, size, and create their own morphology. We study a particular class of active gels, generated by polymerizing actin in the presence of cross-linkers and clusters of myosin as molecular motors, which exhibit large contractions. The relevant mechanics for these highly swollen gels is the result of the interplay between activity and liquid flow: gel activity yields a structural reorganization of the gel network and produces a flow of liquid that eventually exits from the gel boundary. This dynamics inherits lengthscales that are typical of the liquid flow processes. The analyses we present provide insights into the contraction dynamics, and they focus on the effects of the geometry on both gel velocity and fluid flow.

DOI: [10.1103/PhysRevE.00.004600](https://doi.org/10.1103/PhysRevE.00.004600)

I. INTRODUCTION

Self-contractile active gels are usually generated by polymerizing actin in the presence of cross-linkers and clusters of myosin as molecular motors [1–7]. The mechanics of active gels presents interesting characteristics: self-contractions generate internal stresses and stiffen the material, thus driving the network into a highly nonlinear, stiffened regime [2]; morphing from flat to curved geometries can be expected when thin disks of active elastic gels are considered [5]; boundaries affect morphing [3].

A distinctive feature of active gels is the fact that the source that drives the system out of equilibrium is local, rather than at the system's boundaries as in passive gels, where boundary tractions and/or fluxes and changes in the chemical equilibrium of the external ambient are the driving forces [8]. From that, we get the definition of active gels as *soft materials in which detailed balance is broken locally* [9].

The first models of active gels are based on a description of the contraction dynamics within the framework of active generalized hydrodynamics, which deal with gel mechanics, liquid transport, and gel activity [5,8–12]. The characteristics of these model are as follows: (i) the liquid flow is described through the mass conservation law and the Stokes equations; (ii) the overall stress in the gel is decomposed in an elastic

component, borrowed from the linear elasticity, and an active component, which mimics the active contractile stress generated by the embedded motors; (iii) the overall stress satisfies the balance of forces under a friction force resulting from the relative velocity of the gel and liquid components. The friction force and the active stress make gel mechanics, liquid transport, and gel activity fully coupled.

Hydrodynamic models are very accurate in describing the contraction dynamics at the network mesh scale, and less interested in coupling that dynamics with the nonlinear mechanics of active gels, which is strongly affected by the liquid flow and important when the description of shape transitions in active gels is of interest [5]. More recently, the mechanics of active gels has been at the center of a few theoretical studies, set within the framework of nonlinear mechanics. The interactions between elastic stresses and liquid flow have been investigated in the presence of gel activity, which affects the behavior of the material, and they have been included through different approaches [13–15]. The common point of view is that activity provides structural changes of the network, which induce liquid motion within the gel. Differently from generalized hydrodynamics, gel and liquid motion are modeled using the stress-diffusion theory, a refined version of nonlinear poroelasticity where liquid mass conservation governs liquid transport, and Fick's law takes the place of Darcy's law [16–18].

In [13], a dynamic cross-linking mechanism is introduced that drives an evolution of the mechanical stiffness of the polymeric network and brings the system out of thermodynamic equilibrium. The consequent gradient in the chemical potential of the liquid drives the liquid flow in the active gel. In the approach exploited in [14,15] by some of the authors,

*bernheim@bgu.ac.il

†livneg@post.bgu.ac.il

‡paola.nardinocchi@uniroma1.it

§filippo.recrosi@uniroma1.it

||teresi@uniroma3.it

75 gel activity acts as a local time-dependent source of strain,
76 driven by generalized forces, whose action breaks locally the
77 thermodynamic equilibrium of the system.

78 Here, we describe the active gel state in terms of the liq-
79 uid density, the large displacement of the gel, and the active
80 strain, as in [14,15]. In addition, we introduce the relationships
81 between active strains and changes in the natural mesh size
82 of the polymer, defined as the distance between cross-links
83 at zero free-energy; we solve the transient problem for gel
84 disks of different aspect ratio; with reference to those disks,
85 we discuss the regimes of fast and slow liquid transport; we
86 identify the characteristic times of the contraction dynamics;
87 and we study the changes in the overall stress state in gel disks
88 of different aspect ratio.

89 The characteristics of this model are as follows: (i) the
90 liquid flow is described through the mass conservation law,
91 which prescribes the change in liquid concentration in the
92 gel and delivers the liquid velocity relative to the gel; (ii)
93 the total large deformation of the gel is the product of an
94 active component, which mimics the contraction generated by
95 the embedded motors, and an elastic component, following
96 the *active strain* approach, which has already been success-
97 fully exploited to describe morphing and growth in active
98 materials [19–21]; (iii) the overall stress depends on the elastic
99 component through a nonlinear constitutive equation and sat-
100 isfies the balance of forces under zero external force; (iv) the
101 generalized forces driving gel activity satisfy a balance equa-
102 tion, equivalent to a flow rule for the local time-dependent
103 active strain.

104 Finally, it is worth noting that, in the limit of small
105 deformations, the active strain approach yields an overall
106 stress that is the sum of a passive and an active component,
107 as in generalized hydrodynamics [19].

108 The goal of the model is describing the interactions
109 between activity, elasticity, and liquid transport through a
110 boundary value problems with initial conditions. Changes in
111 boundary and initial conditions allow us to model a variety
112 of dynamical phenomena and, hopefully, to inspire further
113 experiments to improve the design of the active characteristics
114 of the gel and of its relevant mechanics.

115 Specifically, we aim to reproduce qualitatively the ex-
116 perimental findings presented in [5], where the contraction
117 dynamics of an active gel disk has been followed and de-
118 scribed in great detail. In doing so, the analysis of the
119 competitive role of gel contractility and liquid flow in driving
120 the mechanics of the active gel is exploited. It is shown that
121 the shortest lengthscale is relevant for the contraction dynamics,
122 whereas the aspect ratio of the disk (diameter to thickness
123 ratio) affects the evolution of the disk size and the stress
124 distribution.

125 In Sec. II, the basic characteristics of the active gel model
126 are presented and contrasted with those of standard passive
127 gels. In Sec. III, liquid flow, stresses, and gel contractions are
128 introduced, and the equations driving the transient behavior
129 of the disks are presented under the cylindrical symmetry
130 hypotheses. In Sec. IV, the steady states of the active gel
131 are presented. In Sec. V, the regimes of fast and slow liquid
132 transport are identified, and the contraction dynamics of active
133 gel disks of different aspect ratios is studied through a set of
134 numerical experiments.

II. POLYMER FRACTION AND ACTIVE VOLUME

Differently from passive polymer gels, active gels have the
ability to *reorganize* their mesh, that is, to reduce their natural
mesh size by means of motor-induced filaments sliding. A
few characteristics of the active and passive gel mechanics are
contrasted here through a simple analysis to highlight the key
elements that can be described by the macroscopic models of
passive and active gels [15,17,18,22–24].

The mechanics of passive polymer gels is commonly
studied within the Flory-Rehner model [25,26]. The model
assumes the free energy to be the sum of an elastic energy
of the network and a mixing energy for the interactions
solvent/network. The elastic energy depends on the stretch
of the polymer chains from the dry conditions through a
nonlinear spring model. The mixing energy depends on the
polymer fraction ϕ , that is, the ratio between the volume V_p
occupied by the polymer and the current volume v of the gel:

$$\phi = \frac{V_p}{v} \quad \text{with} \quad v = V_p + v_l, \quad (1)$$

where v_l is the volume of solvent content. Formula (1) is based
on the assumption that a given mass of polymer occupies a
constant volume V_p , and any change of the current volume v
must be entirely due to the solvent volume v_l . The zero-energy
state, that is, the natural state of the gel, corresponds to the
dry state ($\phi = 1$). Any change in the solvent content, driven
by changes in the chemical potential, stretches the chains,
mixes solvent and polymer, and increases the free energy. The
balance between the mixing energy, which favors swelling,
and the elastic energy, which hampers swelling, yields the
thermodynamic equilibrium state.

Our active gel model uses the same assumptions for the
free energy, but relieves the constraint of a constant polymer
volume. The volume of the polymer can vary because of a
change of the natural length of the mesh size due to the pulling
of molecular motors, and this new volume v_a is named *active
volume*. It is worth noting that V_p and v_a correspond to the
same mass of dry polymer; thus, activity, by changing only
the gel volume v , varies the ratio between the polymer mass
and the overall gel volume, that is, the effective gel density.
Moreover, as liquid is expelled during contraction, gel density
increases, a phenomenon called *densification*. For the active
gel model, the polymer fraction is given by

$$\phi = \frac{v_a}{v} \quad \text{with} \quad v = v_a + v_l. \quad (2)$$

Thus, we may have the same polymer fraction ϕ with different
pairs v_a, v_l :

$$\phi = \frac{v_{a0}}{v_{a0} + v_{l0}} = \frac{v_{a1}}{v_{a1} + v_{l1}} \quad \Rightarrow \quad \frac{v_{a1}}{v_{a0}} = \frac{v_{l1}}{v_{l0}} \quad (3)$$

as $1/\phi = 1 + v_{l0}/v_{a0} = 1 + v_{l1}/v_{a1}$. From (3), it follows that
a contraction of the polymer network yields a proportional
reduction of its solvent content, that is, for $v_{a1} < v_{a0}$ it holds
that $v_{l1} < v_{l0}$. For example, if we have $v_{a0} = 1 \text{ mm}^3$ and
 $v_{l0} = 1000 \text{ mm}^3$, we have $\phi = 1/1001$. We may have the
same polymer fraction ϕ , with a contraction that halves
the polymer volume, that is, $v_{a1} = 0.5 \text{ mm}^3$, and reduces
the solvent content to $v_{l1} = 500 \text{ mm}^3$.

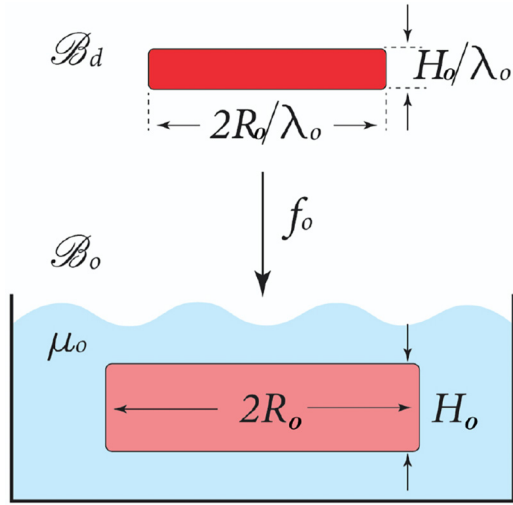


FIG. 1. The disk is dry at the reference configuration \mathcal{B}_d , and swollen at the initial one \mathcal{B}_o . The volume of \mathcal{B}_o is much larger than that of \mathcal{B}_d due to liquid content: H_o and $2R_o$ are the thickness and diameter of \mathcal{B}_o , which are λ_o times larger than the corresponding reference lengths. The initial configuration is given by $x_o = \lambda_o X$, where the stretch λ_o is determined by the bath's chemical potential.

185 The natural state of the active gel corresponds to $\phi = 1$,
 186 and changes in the solvent content can be driven also at con-
 187 stant chemical potential of the bath: liquid flow is generated by
 188 active contraction. We anticipate a key feature of the model: to
 189 maintain a steady gel volume, that is, a volume that remains
 190 constant in time, motor activity is required. This latter is a
 191 distinctive feature of active gels compared to passive ones.
 192 Indeed, passive gels under external loads stay in their equi-
 193 librium state until a change at the system's boundaries occurs.
 194 On the contrary, active gels are brought out of thermodynamic
 195 equilibrium by the action of local molecular motors [8].

196 This key point inspired us. The model presents a new
 197 evolution equation, which describes gel activity; it is driven
 198 by a source term representing the local magnitude of motor
 199 activity, which brings the system out of equilibrium [9]. This
 200 activity in turn generates a solvent flow in the gel: contraction
 201 of the polymer mesh, driven by the motors, yields solvent flow
 202 towards the boundary of the body, favoring its release.

203 We conclude this section by writing the relations between
 204 the average mesh sizes of the gel and its volumes. Continuing
 205 with the example above, the current mesh size ξ is related
 206 to the current gel volume v by $v \sim \xi^3$; likewise, the natural
 207 mesh size ξ_a is related to the active volume v_a by $v_a \sim \xi_a^3$.
 208 Thus, the ratio between the two active volumes v_{a0} and $v_{a1} =$
 209 $v_{a0}/2$ would scale as $\xi_{a1}/\xi_{a0} = (1/2)^{1/3} \simeq 0.8$. Both ξ_a and ξ
 210 may be very different from the reference mesh size ξ_d of the
 211 dry polymer (before contraction acts), i.e., the passive one,
 212 due to activity and liquid flow, as it has been shown in [5]
 213 by fluorescence micrographs of a polymerizing and actively
 214 contracting actomyosin network (see the cartoon in Fig. 2).

215 III. LIQUID FLOWS, STRESSES, AND GEL 216 CONTRACTIONS

217 The active gel model is formulated in the framework of
 218 three-dimensional (3D) continuum mechanics (see [14,15])

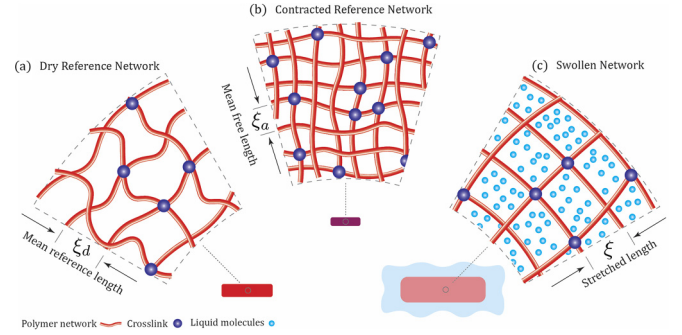


FIG. 2. Schematics of the gel: (a) Dry-reference mesh (red) of size ξ_d with cross-links (blue dots). (b) Dry-contracted mesh: mesh size ξ_a is reduced with respect to ξ_d , and cross-link density is higher. (c) Swollen mesh: liquid molecules (light blue dots) swell the dry-contracted mesh: the free energy is proportional to the stretch ξ/ξ_a between the contracted mesh and the swollen one.

219 for details), which allows us to set up initial-boundary value
 220 problems relevant to describe real experiments. Here, inspired
 221 by the experiments in [5], we consider a disklike continuum
 222 body. At the initial time, the swollen, flat gel disk \mathcal{B}_o has
 223 radius R_o and thickness H_o . Both R_o and H_o are λ_o times larger
 224 than the radius and thickness of the corresponding dry disk
 225 \mathcal{B}_d assumed as a reference configuration of the active gel
 226 disk (see Fig. 1). The model describes the state of the gel
 227 at any material point $X \in \mathcal{B}_d$ and time $\tau \in \mathcal{T}$, with \mathcal{T} the
 228 time interval, by using the following three state variables: the
 229 solvent concentration $c_d(X, \tau)$ per unit of dry volume ($[c_d] =$
 230 mol/m^3), the mechanical displacement $\mathbf{u}_d(X, \tau)$ ($[\mathbf{u}_d] = \text{m}$),
 231 and the active strain tensor $\mathbf{F}_a(X, \tau)$ ($[\mathbf{F}_a] = 1$). To these three
 232 state variables of the model, there correspond three balance
 233 equations, which control liquid flow, stress state, and active
 234 contractions.

235 The current position x of the point X of the gel is given
 236 by $x = X + \mathbf{u}_d(X, \tau)$ and the deformation gradient $\partial x/\partial X$ is
 237 $\mathbf{F}_d = \mathbf{I} + \nabla \mathbf{u}_d$. We denote with \mathcal{B}_τ the current configuration
 238 of the gel at time τ ; the initial configuration \mathcal{B}_o is thus given by
 239 $x_o = X + \mathbf{u}_d(X, 0) = \lambda_o X$, where the stretch λ_o is determined
 240 by the bath's chemical potential.

241 Solvent concentration c_d and displacement \mathbf{u}_d are the stan-
 242 dard state variables of the Flory-Rehner model; the active
 243 strain \mathbf{F}_a is the new variable used to describe the gel contrac-
 244 tion, that is, the local change of the natural shape of the mesh
 245 due to motor activity (see Fig. 2). The tensor \mathbf{F}_a is the 3D local
 246 equivalent of the volume v_a mentioned in the previous section:
 247 given the reference volume element dV_d , the correspond-
 248 ing contracted and current volume elements dv_a and dv are
 249 given by

$$249 \quad dv_a = J_a dV_d \quad \text{and} \quad dv = J_d dV_d, \quad (4)$$

250 with $J_a = \det \mathbf{F}_a$ and $J_d = \det \mathbf{F}_d$. The deformation between
 251 the current and the contracted state is measured by the elastic
 252 deformation $\mathbf{F}_e = \mathbf{F}_d \mathbf{F}_a^{-1}$; see [19,27]. It is worth noting that
 253 no contraction corresponds to $\mathbf{F}_a = \mathbf{I}$, $J_a = 1$, and we recover
 254 the standard stress-diffusion model of passive gels. Moreover,
 255 the time-dependent symmetric tensor $\mathbf{C}_a = \mathbf{F}_a^T \mathbf{F}_a$ corresponds
 256 to the target or natural metric used in [20,21], and the symmetric
 257 tensor $\mathbf{C}_e = \mathbf{F}_e^T \mathbf{F}_e$ describes the so-called elastic metric,
 258 which affects stress distribution in the network [19].

At any point $X \in \mathcal{B}_d$ and time $\tau \in \mathcal{T}$, the solvent content of a volume element is $dv_l = \Omega c_d dV_d$, with Ω the molar volume of the liquid ($[\Omega] = \text{m}^3/\text{mol}$). The requirement that the current volume element dv is the sum of the active volume dv_a plus the liquid volume dv_l , that is, $dv = dv_a + dv_l$, yields an important relation that couples the three state variables of the problem,

$$J_d(X, \tau) = J_a(X, \tau) + \Omega c_d(X, \tau). \quad (5)$$

Looking at the mesh size, we have the same scaling as in the previous 1D example: $dv \sim \xi^3$, $dv_a \sim \xi_a^3$, $\xi_a/\xi_d \simeq J_a^{1/3}$, and $\xi/\xi_d \simeq J_d^{1/3}$.

The polymer fraction ϕ , that is, the ratio between dv_a and dv , is now a function of X and τ , and is given by

$$\phi(X, \tau) = \frac{J_a(X, \tau)}{J_d(X, \tau)} = \frac{1}{J_e(X, \tau)} \quad \text{with} \quad J_e = \det \mathbf{F}_e. \quad (6)$$

In the following, we shall study highly swollen active gels whose polymer fraction $\phi \simeq 10^{-3}$, while J_d ranges between 1000 and 50. Thus, most of the gel volume is due to liquid content, and given the assumption that the mass of the solid matrix remains constant, the gel densification can be measured by the ratio $dv_o/dv = J_{do}/J_d$, where $dv_o = J_{do} dV_d$ is the volume element of the initial configuration \mathcal{B}_o . During the contraction, this ratio becomes much larger than 1, as a large volume of liquid is expelled from the gel. This phenomenon has been observed in experiments [5] and is reproduced by our physical model.

A. Liquid flows

Any gel contraction deforms the gel and drives liquid flow through it; thus, liquid flows within a moving medium. In the spatial frame, the liquid content dv_l of a volume element is described by the current concentration c , defined by $dv_l = \Omega c_d dV_d = \Omega c dv$. From (4), it follows that $c_d = c J_d$. Analogously, the gel velocity \mathbf{u}_d is described by the spatial velocity \mathbf{v} . The local liquid mass conservation in the current configuration is

$$\dot{c} + \text{div}(\mathbf{h} + c\mathbf{v}) = 0 \quad \text{in} \quad \mathcal{B}_t, \quad (7)$$

and it shows that the solvent flux is the sum of a diffusive component \mathbf{h} and a convective component $c\mathbf{v}$, due to gel velocity \mathbf{v} , ($[\mathbf{h}] = [c\mathbf{v}] = \text{mol}/\text{m}^2 \text{ 1/s}$). Equation (7) can be rewritten as follows:

$$\dot{c} + \text{div}(c\mathbf{v}_l) = 0 \quad \text{with} \quad \mathbf{v}_l = \frac{\mathbf{h}}{c} + \mathbf{v}, \quad (8)$$

where \mathbf{v}_l represent the liquid velocity. Hence, the liquid flux \mathbf{h} depends on the relative liquid velocity to the gel as $\mathbf{h} = c(\mathbf{v}_l - \mathbf{v})$. The cartoon in Fig. 3 shows the consequences of Eq. (8) for some values of the relative liquid/gel velocity $\mathbf{v}_l - \mathbf{v}$. The liquid volume-rate $d\dot{v}_l$ through the boundary da of a volume element dv is given by

$$d\dot{v}_l = -\Omega \mathbf{h} \cdot \mathbf{n} da = -\Omega c(\mathbf{v}_l - \mathbf{v}) \cdot \mathbf{n} da. \quad (9)$$

It holds that $d\dot{v}_l > 0$ when liquid is uptaken and $d\dot{v}_l < 0$ when it is expelled. The same volume-rate $d\dot{v}_l$ can be written in the material frame by using a standard pull-back map; we have

$$d\dot{v}_l = -\Omega \mathbf{h} \cdot \mathbf{n} da = -\Omega \mathbf{h}_d \cdot \mathbf{m} dA_d, \quad (10)$$

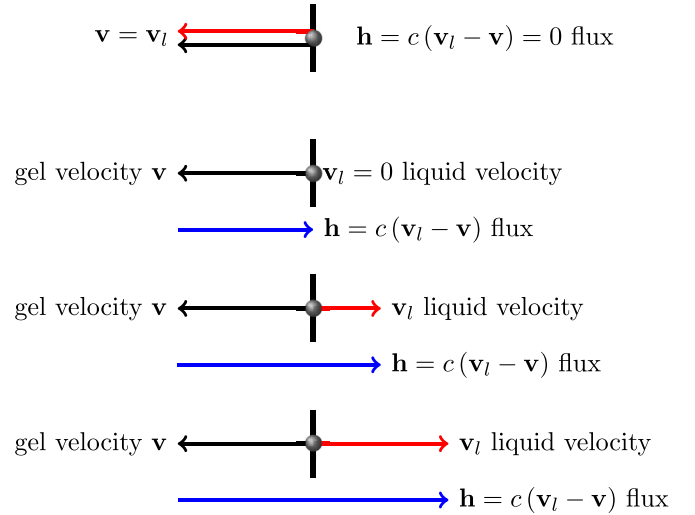


FIG. 3. Given a point (circle) on the boundary (vertical thick line), the current flux \mathbf{h} through the boundary (blue arrow) depends on the relative velocity $(\mathbf{v}_l - \mathbf{v})$. The cartoon shows four cases with different \mathbf{v}_l (red arrow), whose outcome ranges from zero flux (top) to a very large flux (bottom).

with \mathbf{n} and \mathbf{m} the unit normals to the area elements da and dA_d , respectively. Equation (10) yields the definition of the reference flux $\mathbf{h}_d = J \mathbf{F}^{-1} \mathbf{h}$.

Also, the local liquid mass conservation (7), written in the current configuration, can be pulled back from \mathcal{B}_t to \mathcal{B}_d : the corresponding liquid mass conservation written in the material frame \mathcal{B}_d is given by

$$\dot{c}_d + \text{div} \mathbf{h}_d = 0 \quad \text{in} \quad \mathcal{B}_d. \quad (11)$$

Equation (11) is the one we shall use and solve in our model. It is worth noting that by writing the liquid mass conservation in the material frame, it could not be noticed at a glance that the liquid flux \mathbf{h}_d is the sum of a diffusive term plus a convective one.

B. Stresses and active contractions

The overall stress in the current configuration is measured by the Cauchy stress tensor \mathbf{T} , which gives the force $\mathbf{T}\mathbf{n}$ per unit current area da . To \mathbf{T} there corresponds a nominal stress $\mathbf{S}_d = \mathbf{T}\mathbf{F}_d^*/J$, which gives the force $\mathbf{S}_d\mathbf{m}$ per unit reference area dA [therein, $\mathbf{F}_d^* = (\mathbf{F}_d^T)^{-1}$]. The balance equation of forces in the reference configuration \mathcal{B}_d is written in terms of \mathbf{S}_d as

$$\text{div} \mathbf{S}_d = \mathbf{0} \quad \text{in} \quad \mathcal{B}_d \quad \text{and} \quad \mathbf{S}_d \mathbf{m} = \mathbf{0} \quad \text{on} \quad \partial \mathcal{B}_d. \quad (12)$$

The right side of (12) is zero because we are neglecting inertial forces (as timescales associated with diffusion and activity are considerably longer than those associated with inertia). The right side of (12) is zero because we are assuming that the boundary pressure exerted by the liquid in the bath on the gel is negligible, and we do not have any other external boundary tractions.

Balance of forces holds at any time t and, when the liquid flux $\mathbf{h} = \mathbf{0}$, characterizes the thermodynamic equilibrium in passive gels. In active gels we have one more balance equation describing the contraction dynamics. It produces a

335 dissipative dynamics in the form of a flow rule for the local
336 time-dependent active strain \mathbf{F}_a as

$$\dot{\mathbf{F}}_a = \mathbf{M}^{-1}\{[\mathbf{B} - \mathbf{E}_{\text{sh}}(\mathbf{F}, c_d)]\}\mathbf{F}_a, \quad (13)$$

337 where the generalized force \mathbf{B} mimics the action of the molec-
338 ular motors, and the Eshelby tensor \mathbf{E}_{sh} brings in the model the
339 effect of the chemomechanical state of the body. Finally, the
340 power density dissipated in the system due to active contrac-
341 tion is $\mathbf{M}\dot{\mathbf{F}}_a \cdot \mathbf{F}_a$, and the *dissipation tensor* \mathbf{M} is assumed to be
342 positive-definite (to get a positive dissipation power density)
343 and diagonal.

344 C. Model equations under cylindrical symmetry

345 We exploit the cylindrical symmetry that greatly simplifies
346 the evolution equations of the problem; thus, the reference
347 disk \mathcal{B}_d is represented by its vertical cross section \mathcal{S}_d spanned
348 by the radial coordinate $r \in (0, R_d)$ and the vertical one $z \in$
349 $(0, H_d)$. With this, the displacement \mathbf{u}_d has two nonzero com-
350 ponents: the radial u and the vertical w component; within
351 the class of tensors \mathbf{F}_a , which are cylindrically symmetric,
352 we choose a diagonal one and write $\mathbf{F}_a = \text{diag}(\gamma_r, \gamma_\theta, \gamma_z)$.
353 The consequence of this choice is that our active contraction
354 provides a change in the natural mesh size that acts as a
355 local time-dependent source of volumetric and linear strains,
356 whereas shear strains are neglected.

357 The state variables of the problem are reduced to the fol-
358 lowing six scalar fields: the solvent concentration c_d , the two
359 displacements (u, w) , and the three contractions $(\gamma_r, \gamma_\theta, \gamma_z)$;
360 each field is a function of the coordinates (r, z) and the time τ .
361 Moreover, we assume that the derivatives $u_{,z}$ and $w_{,r}$ are zero,
362 that is, we neglect any possible small shearing between the
363 vertical and radial directions. It follows that the deformation
364 gradient \mathbf{F}_d reduces to $\mathbf{F}_d = \text{diag}(\lambda_r, \lambda_\theta, \lambda_z)$ with the radial,
365 hoop, and vertical deformations defined as

$$\lambda_r = 1 + u_{,r}, \quad \lambda_\theta = 1 + u/r, \quad \lambda_z = 1 + w_{,z}, \quad (14)$$

366 respectively. Under the symmetry assumption, the volumetric
367 constraint (5) takes the form

$$\lambda_r \lambda_\theta \lambda_z = 1 + \Omega c_d. \quad (15)$$

368 The state of the active gel is ruled by the set of balance
369 equations introduced above. Under the cylindrical symmetry
370 hypotheses, Eq. (11) reduces to

$$-\dot{c}_d = h_{r,r} + \frac{h_r}{r} + h_{z,z}, \quad [3mm] \quad (16)$$

371 where h_r and h_z are the radial and vertical components of
372 the solvent flux. So, the liquid volume rate through the
373 lateral surface of the disk is $2\pi R_d \Omega h_r(R_d, z) dz$, whereas
374 the liquid volume rate through the top face of the disk is
375 $2\pi r \Omega h_z(r, H_d) dr$. Equations (12) reduce to

$$s_{r,r} + \frac{s_r - s_\theta}{r} = 0 \quad \text{and} \quad s_{z,z} = 0, \quad (17)$$

376 where s_r , s_θ , and s_z are the radial, hoop, and vertical com-
377 ponents of the nominal stress (also called symmetric Piola
378 stress), that is, the stress components on an area element dA_d
379 orthogonal to the radial direction, to the azimuthal direction,
380 and to the vertical direction.

381 Fluxes h_r and h_z , chemical potential μ , and stresses s_r ,
382 s_θ , and s_z are related to the stretches λ_i and the contractions
383 γ_i ($i = r, \theta, z$) by constitutive equations, whose derivation is
384 fully described in several texts and papers (see [16,18,27]).
385 Shortly, liquid transport in the gel is described by a kinetic
386 law, based on the assumption that the liquid molecules move
387 across the gel pores following Fick's law (linear dependence
388 on the chemical potential gradient):

$$h_r = -\frac{D c_d}{RT \lambda_r^2} \mu_{,r} \quad \text{and} \quad h_z = -\frac{D c_d}{RT \lambda_z^2} \mu_{,z}, \quad (18)$$

389 where D is the diffusion coefficient, which has been assumed
390 to be the same in the radial and vertical directions, R and T are
391 the gas constant and the temperature, respectively, and $\mu =$
392 $\mu(J_e, p)$ is the chemical potential of the solvent in the gel:

$$\mu = RT g(J_e) + \Omega p, \quad J_e = \det \mathbf{F}_e = \frac{J_d}{J_a}, \quad (19)$$

393 with

$$g(J_e) = \left[\log \left(\frac{J_e - 1}{J_e} \right) + \frac{1}{J_e} + \frac{\chi}{J_e^2} \right]. \quad (20)$$

394 Therein, the parameter χ is the nondimensional disaffinity
395 parameter, which controls the attraction between liquid and
396 network, and the pressure field p is the Lagrangian mul-
397 tiplier of the constraint $J_d = J_a + \Omega c_d$ [Eq. (5)] [22]. The
398 characteristic time $l^2/D = \tau_d$ of the liquid transport, with l
399 a characteristic length of the problem, will be compared with
400 the characteristic times brought in the model by contraction
401 dynamics to identify different regimes.

402 Finally, the overall stresses are given by constitutive equa-
403 tions of the form

$$\begin{aligned} s_r &= G \lambda_r \frac{\gamma_\theta \gamma_z}{\gamma_r} - p \lambda_\theta \lambda_z, \\ s_\theta &= G \lambda_\theta \frac{\gamma_r \gamma_z}{\gamma_\theta} - p \lambda_r \lambda_z, \\ s_z &= G \lambda_z \frac{\gamma_r \gamma_\theta}{\gamma_z} - p \lambda_r \lambda_\theta, \end{aligned} \quad (21)$$

404 where G is the shear modulus of the dry polymer network
405 ($[G] = \text{J/m}^3$). The corresponding Cauchy stresses are $\sigma_r =$
406 $s_r/\lambda_\theta \lambda_z$, $\sigma_\theta = s_\theta/\lambda_r \lambda_z$, and $\sigma_z = s_z/\lambda_r \lambda_r$.

407 Finally, Eq. (13) specializes to three scalar equations,
408 which deliver the flow rules for the active contractions γ_i
409 ($i = r, \theta, z$) [28]:

$$\begin{aligned} \dot{\gamma}_r &= \frac{1}{\eta_r} (\beta_r - E_r) \gamma_r, \\ \dot{\gamma}_\theta &= \frac{1}{\eta_\theta} (\beta_\theta - E_\theta) \gamma_\theta, \\ \dot{\gamma}_z &= \frac{1}{\eta_z} (\beta_z - E_z) \gamma_z. \end{aligned} \quad (22)$$

410 These equations show that flow rules are driven by $(\beta_i - E_i)$
411 ($i = r, \theta, z$), that is, by the difference between the generalized
412 forces β_i and the components E_i of the Eshelby tensor, which
413 depends constitutively on the chemomechanical state of the
414 gel. We assume $\beta_i(X, \tau) = \beta(\tau)$, corresponding to assuming
415 an isotropic and homogeneous distribution of motors in the
416 gel, and we view it as the control parameter of the contraction

417 process. On the contrary, we cannot control the components
418 E_i , which are in general neither homogeneous nor constant
419 and, within the Flory-Rehner thermodynamics, depend on the
420 state of the gel as

$$E_i = e_y - J_d \sigma_i \quad (i = r, \theta, z) \quad (23)$$

421 with

$$e_y = \frac{RT}{\Omega} J_a F(\mathbf{C}_e) - c_d \mu(J_e, p). \quad (24)$$

422 The function $F(\mathbf{C}_e)$ is the dimensionless free-energy density
423 per unit natural volume, and it reads $F(\mathbf{C}_e) = f_c(J_e) +$
424 $m f_e(\mathbf{C}_e)$, with f_c and f_e the dimensionless mixing and elastic
425 free-energy, where $m = G\Omega/RT$ is the ratio between the
426 elastic energy and the mixing energy:

$$f_c(J_e) = (J_e - 1) \log\left(1 - \frac{1}{J_e}\right) + \chi \left(1 - \frac{1}{J_e}\right),$$

$$f_e(\mathbf{C}_e) = \frac{1}{2} (\text{tr} \mathbf{C}_e - 3). \quad (25)$$

427 Equations (22)–(25) show that the interplay between activity,
428 elasticity, and liquid transport depends on the effective controls
429 $(\beta - E_i)$; in general, the dissipation constants η_i can be
430 different in the three directions and can bring in the model
431 more than one characteristic time $\tau_{\eta_i} = \eta_i/RT/\Omega$; large dissipation
432 constants yield small contraction time rates $(\dot{\gamma}_r, \dot{\gamma}_\theta, \dot{\gamma}_z)$,
433 under the same effective input.

434 We assume that the disk is not constrained, nor loaded, the
435 entire disk boundary is permeable, and chemical equilibrium
436 holds at the boundary, that is,

$$\mu = \mu_e \quad \text{on} \quad \partial \mathcal{S}_d, \quad (26)$$

437 where μ_e is the difference between the chemical potential
438 of the bath and that of pure water ($\mu_e = 0$ corresponds to a
439 pure water bath). Finally, the initial conditions for the dis-
440 placements u, w , the concentration c_d , and the contractions
441 γ_i ($i = r, \theta, z$) are the following:

$$u = (\lambda_o - 1)r, \quad w = (\lambda_o - 1)z, \quad c_d = c_{d0}, \quad \gamma_i = 1, \quad (27)$$

442 corresponding to the deformation $f_o(X) = \lambda_o X$ for any $X \in$
443 \mathcal{B}_d from \mathcal{B}_d to \mathcal{B}_0 (see Fig. 1).

444 IV. INITIAL AND FINAL EQUILIBRIUM STATES

445 The controls μ_e and β trigger contraction-liquid transport
446 dynamics between the initial and the final state (see Fig. 4).
447 We assume that both μ_e and β have a characteristic evolution
448 dynamics from their initial values (μ_0, β_0) to their final values
449 (μ_1, β_1) , described by the following time laws:

$$\mu_e = \mu_e(\tau) = \mu_0 + (\mu_1 - \mu_0) s(\tau/\tau_\mu),$$

$$\beta = \beta(\tau) = \beta_0 + (\beta_1 - \beta_0) s(\tau/\tau_\beta), \quad (28)$$

450 where $s(\cdot)$ is a smoothed step function [29] running from 0
451 to 1 in the interval (0,1), and τ_μ and τ_β are characteristic
452 times [30], which have been tuned to match the results pre-
453 sented in [5]; see Table I. For the motors, the characteristic
454 time depends on the binding/unbinding kinetics of the motors
455 to the actin filaments, whereas for the chemical potential, the

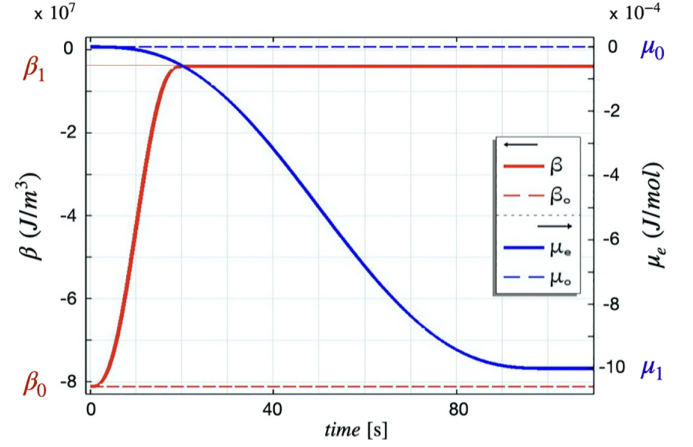


FIG. 4. β goes from β_0 to β_1 in $\tau_\beta = 20$ s (dashed and solid red lines); μ stays constant in scenario (a) and goes from $\mu_0 = 0$ to μ_1 in $\tau_\mu = 100$ s (solid blue). β axis at left, μ axis at right.

characteristic time reflects the mixing kinetic of possibly free
biopolymer chains and the liquid in the bath.

The initial state and the final one are *equilibrium states*,
that is, $\mathbf{h}_d = \mathbf{0}$, which implies $\dot{c}_d = 0$ and $\dot{\gamma}_i = 0$ ($i = r, \theta, z$).

We assume that at the initial and final equilibrium states,
 \mathbf{F}_d and \mathbf{F}_a are uniform and spherical, that is, $\mathbf{F}_d = \lambda \mathbf{I}$, $\mathbf{F}_a =$
 $\gamma \mathbf{I}$, and that the overall stress is null. With this, and with
Eqs. (21), (19), and (23), we can represent the chemical po-
tential and the Eshelby components at those equilibrium states
as functions of $J_a = \gamma^3$ and $J_d = \lambda^3$:

$$\mu = \mu(J_d/J_a) = \mu(J_e) \quad \text{and} \quad E_i = e_y(J_a, J_e). \quad (29)$$

Moreover, the equilibrium states are guaranteed by constant
and homogeneous chemical potential μ_e and bulk source β
such that

$$\mu_e = \mu \quad \text{and} \quad \beta = E_i. \quad (30)$$

Equations (29) and (30) deliver the relation between the pair
 (J_a, J_d) and the pair (μ_e, β) which must hold at the equilib-
rium states:

$$\mu_e = \mu(J_e) \quad \text{and} \quad \beta = e_y(J_a, J_e). \quad (31)$$

TABLE I. Material and geometrical parameters.

Shear modulus	$G = 135$ Pa
Flory parameter	$\chi = 0.4$
Water molar volume	$\Omega = 1.8 \times 10^{-5}$ m ³ /mol
Temperature	$T = 293$ K
Energy ratio	$m = G\Omega/RT = 1 \times 10^{-6}$
Diffusivity	$D = 1 \times 10^{-3}$ m ² /s
Dissipation	$\eta = 1 \times 10^5$ Pa s
Initial radius	$R_o = 1500$ μ m
Initial swollen volume and stretch ratio	$J_o = 1000$, $\lambda_o = 10$
Initial aspect ratio	$AR = 2 R_o/H_o = 20$ – 40
Initial thickness	$H_o = 150$ – 75 μ m
Final volume/initial volume	$J_{a1} = 0.05$
Control time for β	$\tau_\beta = 20$ s
Control time for μ	$\tau_\mu = 100$ s

We label (J_{d0}, J_{a0}) the pair corresponding to the initial equilibrium state and (J_{d1}, J_{a1}) the pair corresponding to the final state; the same labels hold for all the other quantities.

1. Material parameters

The values assigned to the initial thickness and aspect ratio (AR) have been prompted by [5], and the successive parametric analyses always consider values of AR and H_o not too far from the initial ones. The discrepancy between our value for the shear modulus G and the value reported in [5] is due to the fact that the former is the shear modulus at dry conditions, while the latter is the effective shear modulus G_{eff} measured at the swollen state, with $G_{\text{eff}} \simeq G/J_{d0}^{1/3}$. We set the diffusivity constant D and the dissipation $\eta_r = \eta_\theta = \eta_z = \eta$ in order to get a time evolution from \mathcal{B}_o to \mathcal{B}_1 similar to that taken by the real disk to reach a mechanically stable state (steady state), that is, ~ 200 s. With this, we set the characteristic time τ_η , leaving τ_d free to get different values, depending on H_o , which are in any case always higher than τ_η (see Table I for the complete list of material parameters).

2. Initial state

We assume a fully swollen state as the initial state of the gel, characterized by a not contracted mesh size ξ_a equal to the reference mesh size ξ_d . From an experimental point of view, it means that self-contraction and liquid release are going to be initiated; from the modeling point of view, it means that the active gel is still not contracted and is in its thermodynamic equilibrium, that is,

$$\mu_e(0) = \mu_0 = 0 \text{ J/mol} \quad \text{and} \quad J_{a0} = 1. \quad (32)$$

By putting these values in Eqs. (31), we find the initial change in volume $J_{d0} = J_{e0} = \lambda_0^3$ of the gel and the initial value β_0 of the generalized force which maintains that initial state. Specifically, Eqs. (31) take the form

$$0 = \mu(J_{d0}/J_{a0}) \quad \text{and} \quad \beta_0 = e_y(J_{a0}, J_{e0}). \quad (33)$$

The zero stress condition at the initial time delivers $p_0 = G/\lambda_0$. With this, the constitutive Eqs. (19) and (20) for the chemical potential and Eq. (33) deliver

$$0 = \left[\log \left(1 - \frac{1}{\lambda_0^3} \right) + \frac{1}{\lambda_0^3} + \frac{\chi}{\lambda_0^6} \right] + \frac{m}{\lambda_0}. \quad (34)$$

Equation (34) can be solved for λ_0 , and Eq. (33) determines the initial value β_0 which the control has to get to guarantee null contraction ($\xi_a = \xi_d$) and the free swelling stretch λ_0 :

$$\frac{\Omega}{RT} \beta_0 = (\lambda_0^3 - 1) \left(\frac{\lambda_0^3 - 1}{\lambda_0^6} \chi - \frac{1}{\lambda_0^3} \right) + m \left(\frac{1}{\lambda_0} + \frac{\lambda_0^2}{2} - \frac{3}{2} \right). \quad (35)$$

It is worth noting that Eq. (34) is standard in stress-diffusion theories based on Flory-Rehner thermodynamics [25,26]; it is easy to verify that, given μ_0 , the free-swelling stretch λ_0 increases as m decreases. On the contrary, Eq. (35) does not belong to standard stress-diffusion theory, and it is peculiar to the present augmented model.

The initial values of J_d , J_e , c_d , p , and β , corresponding to the material parameter in Table I, can be easily evaluated. In particular, we get $J_{d0} = 1000$.

3. Final states

We consider two different scenarios: (a) where only a change in the generalized force drives the active contractions and liquid transport, that is, $\beta_1 \neq \beta_0$ and $\mu_1 = \mu_0$; (b) where also a change in the chemical potential of the bath drives the active contractions and liquid transport, that is, $\beta_1 \neq \beta_0$ and $\mu_1 \neq \mu_0$.

The differences between the two scenarios are noteworthy. Indeed, in passive gels the input that drives the system out of equilibrium is at the system's boundaries, that is, a change of the chemical potential in the bath starts liquid transport. On the contrary, a distinctive feature of active gels is the fact that the input that drives the system out of equilibrium is local. Through the analysis of the two scenarios, we compare dynamics due to only local input, that is, a change in the generalized force, and to both local and boundary input, that is, a change in both the generalized force and the chemical potential of the bath.

In both the scenarios, however, and in accordance with the experiments in [5], we assume that at the final state the mesh is contracted by $\xi_a/\xi_d = J_{a1}^{1/3} \simeq 0.38$ with respect to the dry mesh size, that is, $J_{a1} = (\xi_a/\xi_d)^3 = 0.05$. The estimation of the final value J_{a1} allows us, within the model, to estimate the final value β_1 of the generalized force, as is shown below by describing step-by-step the procedure to infer those data from the equations of the model.

Scenario a (fluid flow induced by active contractility). We assume

$$\mu_1 = \mu_0 = 0 \text{ J/mol}, \quad J_{a1} = 0.05, \quad (36)$$

and we put these values in Eqs. (31) to obtain the final swelling ratio J_{d1} and the generalized force β_1 . Specifically, the two equations take the form

$$0 = \mu(J_{d1}/J_{a1}) \quad \text{and} \quad \beta_1 = e_y(J_{a1}, J_{e1}). \quad (37)$$

With our data, we find $J_{d1} = 50$. Comparing this value with the change in volume delivered under the same chemical conditions, that is, $J_{d0} = 1000$, we can conclude that, due to self-contraction, an effective bulk stiffening is predicted by the model, as has already been recognized as crucial in other works [10].

Scenario b (fluid flow generated by the active contractility and changes in the chemical potential of the liquid bath). Typically, in the experiments, the chemical potential of the bath is not controlled. While previously assumed constant [see (a)], it is possible that chains, small fragments, and even monomers can be broken from the gel and released into the solution upon contraction of the gel, by changing the chemical potential of the bath [31]. This motivated our choice to study the impact of a change in μ_e on the contraction dynamics.

We assume that at the final equilibrium state, J_{d1} is half the value of case (a), while J_{a1} is the same as before, that is,

$$J_{d1} = 25, \quad J_{a1} = 0.05. \quad (38)$$

TABLE II. Data about the aspect ratios; values of R_o and H_o are in mm.

Constant R_o $H_o(R_o = 1.5)$	Constant H_o $R_o(H_o = 0.1)$	AR
0.15	1.0	20
0.12	1.25	25
0.1	1.50	30
0.086	1.75	35
0.075	2.0	40
0.066	2.25	45

By putting these values in Eqs. (31), we obtain the pair (μ_1, β_1) . Specifically, the two equations take the form

$$\mu_1 = \mu(J_{d1}/J_{a1}) \quad \text{and} \quad \beta_1 = e_y(J_{a1}, J_{e1}). \quad (39)$$

Of course, other choices would be possible; for example, apart from setting different values for J_{d1} , we could first set μ_1 and then determine J_{d1} from Eqs. (31). What we aimed to remark is that the same value of β_1 can deliver a quite different value of the final change in volume J_{d1} of the disk (25 versus 50) when liquid transport and release is driven by both the mesh contraction and the change in the chemical conditions of the bath.

V. CONTRACTION DYNAMICS

Gel activity does not have any characteristic lengths, since motor activity is assumed to be homogeneous across the system. However, contraction dynamics inherits the characteristic length of the dynamic of liquid transport. The disks built and tested in [5] represent a good basis for a pilot study aimed to discuss the relations between the two dynamics in terms of the key geometrical parameter, which is the aspect ratio of the disks.

We carried on the analysis by either changing the disk initial thickness H_o , for a fixed initial disk radius $R_o = 1.5$ mm, or by varying the disk initial radius at a fixed thickness $H_o = 0.10$ mm. The investigated range of parameter AR is described in Table II: it goes from disks of initial aspect ratio 20 (thick disks) to disks of initial aspect ratio 45 (thin disks).

We show the results obtained for gel disks that contract due to motor only [so-called scenario (a)]. All the experiments start with $J_{d0} = 1000$, i.e., at a highly swollen initial state, and $J_{a0} = 1$, and they evolve towards their final steady values $J_{d1} = 50$ and $J_{a1} = 0.05$. As stated above, these values correspond to a reduction in mesh size $= \xi_{a1}/\xi_{a0} = 0.05^{1/3} = 0.38$, where ξ_{a1} represents the final mesh size, and, as stated above, we consider the final state to be stress-free.

In the regime under study, the system reaches its final steady state after $\tau_1 \simeq 200$ s, that is, we have $\tau_\beta \ll \tau_1$ and the dynamics is ruled by the redistribution of water across the gel mesh until its eventual expulsion through the disk boundary.

A. Diffusion-limited regime

Given the equations of the model, there are different characteristic times whose values have an influence on the

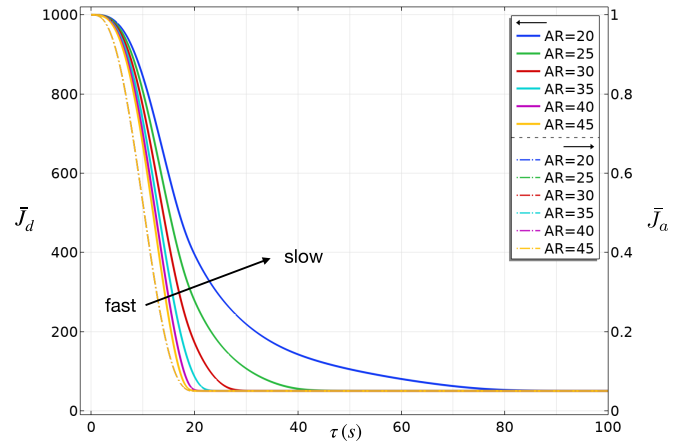


FIG. 5. Plot of \bar{J}_d (solid) and \bar{J}_a (dashed) vs time for different values of AR; disk geometry is given in the first column of Table II. Being $\tau_\eta \ll \tau_\beta$, all the \bar{J}_a curves (dashed) are superimposed, as \bar{J}_a evolves at the same pace of β , and this evolution is not affected by AR. The \bar{J}_d curves (solid) depends strongly on AR, and the thicker the disk, the slower the volume change. This is a consequence of the fact that the liquid must exit through the boundary, and the thickness is the important geometric parameter within our range of AR.

different solution regimes. In particular, the characteristic time τ_η which governs mesh contraction is not size-dependent, being $\tau_\eta \propto \eta \Omega / RT$, while the characteristic time τ_d which governs liquid transport has a length scale, which for our geometries is the current height H , that is, $\tau_d \propto H^2 / D$. Given our choice of η , we have $\tau_\eta \simeq 10^{-3}$ s; the estimation of a value for τ_d is much more difficult because of the large size-change experienced by the disks during contraction.

Our experiments shows that, for our choice of parameters and geometry, the contraction dynamics is *diffusion-limited*, as is affected by the lengthscale. The opposite regime, the so-called *motor-limited* regime, can be realized when $\tau_d \ll \tau_\eta$. The simplest way to discuss the different regimes is through the analysis of the flow rule for J_a , which can be easily derived from Eqs. (22)–(24). Cylindrical symmetry implies

$$J_a = \gamma_r \gamma_\theta \gamma_z \quad \text{and} \quad \dot{J}_a = J_a \left(\frac{\dot{\gamma}_r}{\gamma_r} + \frac{\dot{\gamma}_\theta}{\gamma_\theta} + \frac{\dot{\gamma}_z}{\gamma_z} \right). \quad (40)$$

With this, the flow rule for J_a can be derived from those for γ_i by Eqs. (22), and it takes the form

$$\dot{J}_a = \frac{1}{\eta} [3(\beta - e_y) + J_d \text{tr} \mathbf{T}] J_a. \quad (41)$$

Equation (41) and the equation governing the dynamics of diffusion allow us to discuss some of the evidences of our numerical experiments.

To discuss contraction dynamics, we define the averages $\bar{J}_d(\tau)$ and $\bar{J}_a(\tau)$ of $J_d(r, z, \tau)$ and $J_a(r, z, \tau)$, respectively, which well represent the main features of the phenomenon under study, and give a global glance at the contraction dynamics. Due to the cylindrical symmetry of the system, both averages are evaluated on the two-dimensional domain \mathcal{S}_d of area $R_d \cdot H_d$.

In Fig. 5, we plot \bar{J}_a (dashed) and \bar{J}_d (solid) versus time for different values of AR; the figure shows two major findings.

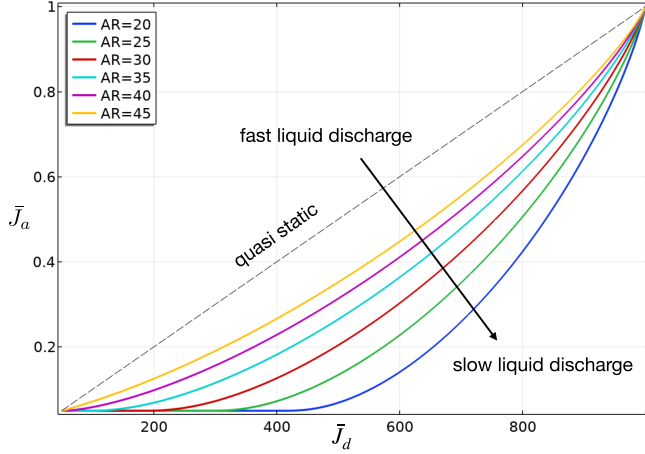


FIG. 6. Plane (\bar{J}_d, \bar{J}_a) : evolution path at constant radius $R_o = 1.5$ mm for different values of AR; disk geometry is given in the first column of Table II. Lower AR correspond to the evolution path far from equilibrium; higher AR corresponds to paths that tend to the quasistatic stress (dashed line).

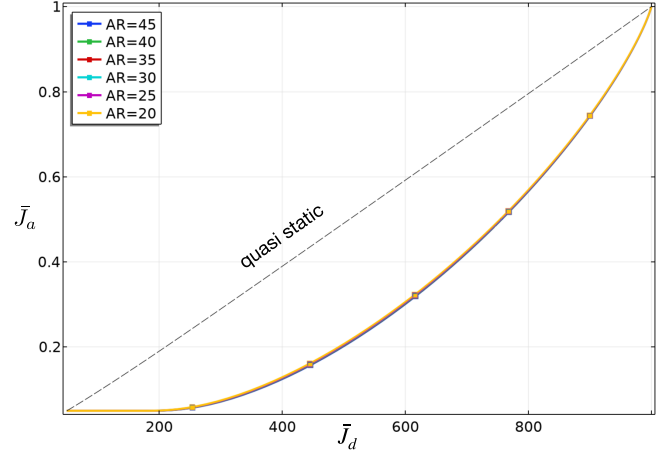


FIG. 7. Plane (\bar{J}_d, \bar{J}_a) : evolution path at constant thickness $H_o = 0.1$ mm for different values of AR; disk geometry is given in the second column of Table II. All the paths are superimposed and the master curve is the one corresponding to AR = 30 in Fig. 6.

636 First, all the curves for \bar{J}_a are superimposed, as $\tau_\eta \ll \tau_\beta$, that
 637 is, the evolution of β is slow with respect to the characteristic
 638 time τ_η , and $\bar{J}_a(\tau)$ has the same dynamics of $\beta(\tau)$; in partic-
 639 ular, the evolution of \bar{J}_a can be approximated as a sequence
 640 of equilibrium problems, which depend on β . Moreover, as
 641 contraction is a local mechanism, this dynamics is much faster
 642 than diffusion, and it is not affected by AR.

643 Secondly, the curves for \bar{J}_d , representing the volume
 644 change, strongly depend on AR, and the thicker the disk, the
 645 slower the volume change. This is a consequence of the fact
 646 that the liquid must exit through the boundary, and for the
 647 range of AR under investigation, the thickness is the important
 648 geometric parameter.

B. Dynamics in the plane (\bar{J}_d, \bar{J}_a)

649 We now focus on the evolution paths in the plane (\bar{J}_d, \bar{J}_a)
 650 for scenario (a), that is, $\mu_e = \mu_o = \text{const}$. In this plane, a
 651 quasistatic stress-free path is represented by a straight line at
 652 constant $\bar{J}_e = \bar{J}_d/\bar{J}_a$, and the dashed line in Figs. 6 and 7. This
 653 path corresponds to a sequence of equilibrium states where
 654 the current swollen volume \bar{J}_d corresponds to a free swelling
 655 for a dry mesh whose current natural volume is \bar{J}_d .

656 Due to the choices made in Table I, which yields a
 657 diffusion-limited regime, liquid transport is affected by the
 658 lengthscale. Thus, thinner disks (higher AR) show an evolu-
 659 tion in the plane that is closer to the stress-free path, that
 660 is, under the same contraction dynamics, liquid transport is
 661 faster for these disks, which can quickly recover the original
 662 stress-free state. On the contrary, for thicker disks (lower AR),
 663 the evolution path is very far from the quasistatic regime:
 664 namely, motor-induced contraction is faster than the water
 665 transport across the gel mesh, which makes the thick gels
 666 highly stressed during their evolution.

667 We investigated the evolution paths for different AR for
 668 varying H_o at constant R_o (Fig. 6) and varying R_o at constant
 669 H_o (Fig. 7). In the first case, Fig. 6 shows that by increasing
 670 the thickness H_o , that is, the characteristic lengthscale across

672 which water flows, it increases the characteristic timescale of
 673 water transport (from yellow to blue solid lines). As $\tau_\eta \gg \tau_d$
 674 for any values of H_o , the quasistatic path is never realized;
 675 however, the thinner the disk is, the closer is the evolution
 676 path to the quasistatic one.

677 To confirm our expectations that the important lengthscale
 678 for water exit is H_o , we also studied disk geometries having
 679 constant thickness and varying radius. Figure 7 shows the
 680 results for the same range of AR: it might be noticed that all
 681 the curves are now superimposed as, being that the shortest
 682 lengthscale H_o is constant, AR has no effect on the dynamics.

C. Gel contraction velocity

683 We studied the contraction velocity of the lateral boundary
 684 of the disk, i.e., the radial velocity and the effects of AR on it.
 685 To do so, we evaluate the average radial stretch Λ_r as follows:
 686

$$\Lambda_r(\tau) = 1 + \frac{1}{H_d} \int_0^{H_d} \frac{u(R_d, z, \tau)}{R_d} dz; \quad (42)$$

687 it is easy to verify that the average stretch Λ_r also corresponds
 688 to the average $\bar{\lambda}_r(\tau)$ of the radial deformation $\lambda_r(r, z, \tau)$ on the
 689 cross section \mathcal{S}_d of area $R_d \cdot H_d$.

690 We also defined an average current radius $R(\tau)$ and a radial
 691 contraction velocity $\dot{R}(\tau)$ with the formulas

$$R(\tau) = \Lambda_r(\tau)R_d \quad \text{and} \quad \dot{R}(\tau) = \dot{\Lambda}_r(\tau)R_d. \quad (43)$$

692 It follows from (43) and the definition of AR that the radial
 693 velocity can also be rewritten as $\dot{R}(\tau) = \dot{\Lambda}_r(\tau) \frac{H_d}{2} \text{AR}$. The
 694 radial velocity $\dot{R}(\tau)$ is always negative, as the gel disk is
 695 contracting and negative is also the generalized force β that
 696 produces a contraction. So, in both Figs. 8 and 9 we repre-
 697 sented $-\dot{R}(\tau)$ and $-\beta/\beta_0$.

698 Figure 8 shows that, for a constant radius, the radial veloc-
 699 ity $\dot{R}(\tau)$ is characterized by two timescales, one for the time
 700 interval during which the velocity increases, and the second
 701 for the following interval where the velocity decreases. In
 702 the first time interval, the curves fit to a linear law, that
 703 is, $\dot{R}(\tau) \propto \tau/\tau_r$, with τ_r the characteristic time of rising.

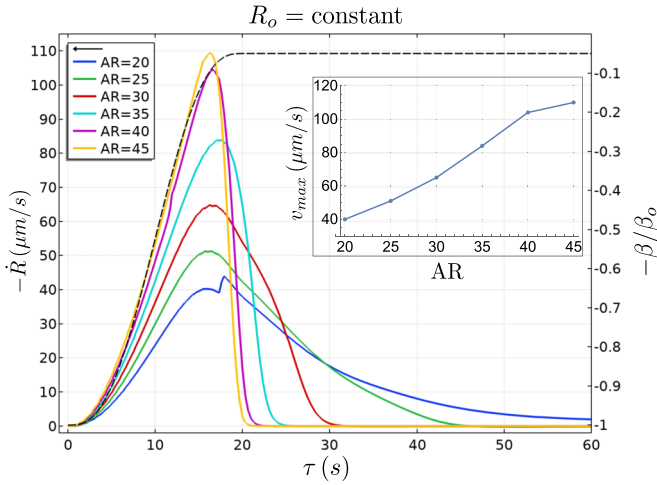


FIG. 8. The time evolution of β (dashed) and corresponding radial contraction velocity \dot{R} of the lateral boundary of the disk at constant radius $R_o = 1.5$ mm for different values of AR; disk geometry is given in the first column of Table II. The color code is the same as in Figs. 6 and 7. The small wiggle in the blue line at $\tau \simeq 17$ s is due to a mechanical buckling: the disk departs from the flat shape; see Fig. 12, panel (c). Velocity ranges over the left vertical axis and β/β_o over the right vertical axis.

704 During the decreasing time interval, curves fit to an exponential law $\dot{R}(\tau) \propto v_{\max} \exp(-\tau/\tau_{\text{decay}})$, with τ_{decay} the characteristic time of decay. The characteristic times of rising and decay have been estimated for any aspect ratio and are listed in Table III.

709 The inset in Fig. 8 shows that the maximum radial velocity v_{\max} , attained at peak time τ_p , depends on the geometric parameter AR [32].

712 Actually, the analysis of Eqs. (42) and (43) shows that when AR changes with H_d (or, equivalently, with H_o as the

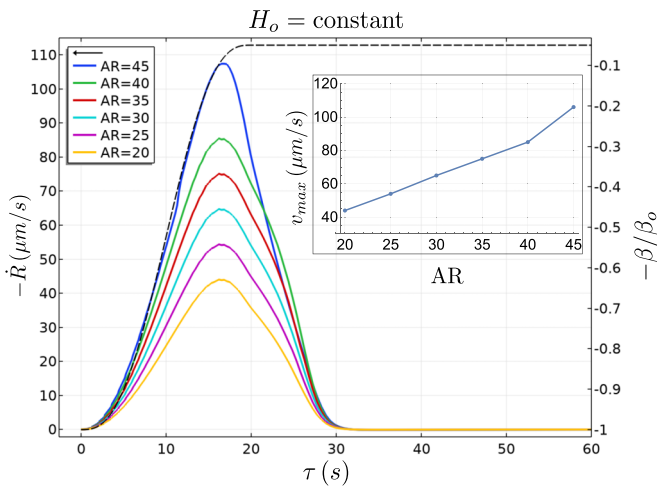


FIG. 9. The time evolution of β (dashed) and corresponding radial contraction velocity \dot{R} of the lateral boundary of the disk at constant thickness $H_o = 0.1$ mm for different values of AR; disk geometry is given in the second column of Table II. Color code is the same as in Figs. 6 and 7. Velocity ranges over the left vertical axis and β/β_o over the right vertical axis.

TABLE III. Max velocity v_{\max} , peak time τ_p , rising time τ_r , and decay time τ_{decay} for different values of aspect ratio AR.

AR	v_{\max} ($\mu\text{m/s}$)	τ_p (s)	τ_r (s)	τ_{decay} (s)
20	44	$\simeq 16$	0.22	13
25	52	$\simeq 16$	0.22	13
30	74	$\simeq 17$	0.18	8
35	84	$\simeq 17$	0.14	3
40	104	$\simeq 17$	0.12	2
45	111	$\simeq 17$	0.11	1.5

initial free-swelling is homogeneous), with R_o constant, the dependence of \dot{R} on AR is also affected by H_d and cannot be linear. The same equations show that, for H_d constant, the dependence of \dot{R} on AR is simply linear. This is what the inset in Fig. 9 shows for the maximum velocity v_{\max} relative to the study at varying radius.

We can split the average stretch Λ_r into an elastic component Λ_e and an active component Λ_a , related to the analogous decomposition of the deformation gradient $\mathbf{F} = \mathbf{F}_e \mathbf{F}_a$ and of the radial deformation λ_r . Thus, the stretching velocity $\dot{\Lambda}_r$ can be written as the sum of two terms, and the radial velocity \dot{R} is represented by

$$\dot{R} = (\dot{\Lambda}_a \Lambda_e + \Lambda_a \dot{\Lambda}_e) R_d, \quad (44)$$

where Λ_a is the average of the active radial deformation γ_r , and it depends on self-contraction, while Λ_e is the average of the elastic radial deformation λ_r/γ_r , and it depends on liquid transport.

Equation (44) highlights the existence of two timescales for \dot{R} : for $\tau < \tau_\beta$ the stretching velocity is dominated by the time evolution of $\beta(\tau)$, while for $\tau > \tau_\beta$ it is dominated by liquid transport, that is,

$$\dot{R} \simeq \dot{\Lambda}_a \Lambda_e R_d \quad \tau < \tau_\beta, \quad (45a)$$

$$\dot{R} \simeq \Lambda_a \dot{\Lambda}_e R_d \quad \tau > \tau_\beta. \quad (45b)$$

Equation (45a) shows that for $t < \tau_\beta = 20$ s, the radial velocity \dot{R} changes with the same rate of Λ_a , which in turns depends on β , as Figs. 8 and 9 show (compare the colored lines with the dashed black line in both figures).

On the other side, Eq. (45b) shows that for $t > \tau_\beta = 20$ s, the radial velocity \dot{R} changes with the rate of Λ_e , which depends on liquid transport and on the smallest lengthscale of the disk, which in our case is H_o , as a comparison between Figs. 8 and 9 shows. The same pair of figures also show clearly that the maximal velocity is reached when τ approaches τ_β , that is, when contraction is near to its maximum value—as was suggested in [5] [see Fig. 4(f) in [5]].

Finally, it is worth noting that the active control β , needed to change the target mesh size, does not change further once it has taken its maximal value. Beyond that, the system evolves towards its steady state by releasing liquid until a new free swollen configuration is reached; at this final state, the effects of the network elasticity balance the active control.

We conclude this section by showing a comparison with experimental results obtained for a very thin disk with AR = 50. By properly tuning the diffusivity D and the dissipation η , our theoretical model is able to reproduce quite

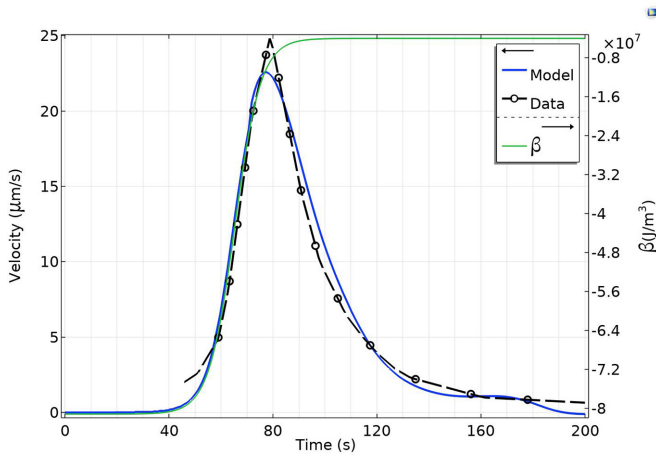


FIG. 10. Radial contraction velocities vs time. Radial \dot{R} (solid blue) contraction velocity of the disk compared with experimental data (dashed with markers). Disk geometry: $R_o = 1.5$ mm, $AR = 50$; material parameters: $D = 0.951 \times 10^{-4}$ m²/s, $\eta = 1.51 \times 10^5$ Pa s.

well the time course of the radial contraction velocity \dot{R} . Figure 10 compares the predicted results (solid-blue) with the experimental ones (dashed-black, circle markers).

D. Densification and stress distribution

As observed in [5], the network starts contracting from the boundary, and the actual mesh size starts decreasing from the boundary to the center of the gel disk. This contraction mode yields boundary effects, which are detected on the gel density, defined as the ratio between the polymer mass and the overall gel volume, and on the overall stress state in the disk.

In [5], a gel densification was observed, that is, an increase of the gel density starting at the periphery and propagating into the gel interior.

Within the model, we use the ratio J_{d0}/J_d to measure the densification from the initial state. Figure 11 shows the den-

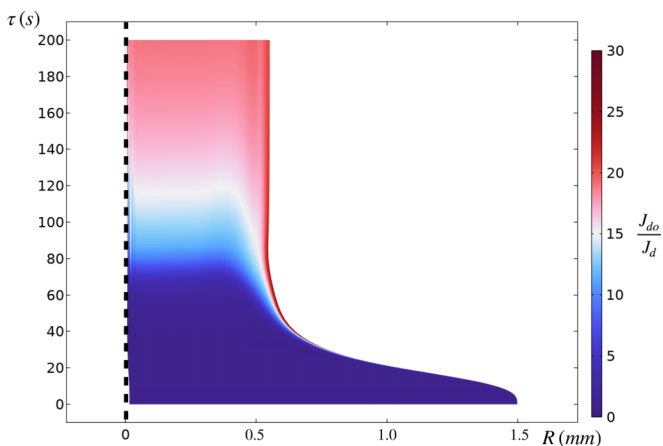


FIG. 11. Densification at the middle cross section of the disk. Ratio J_{d0}/J_d in the plane (R, τ) ; color map: blue is more wet, red is more dry. Densification (red color) starts at the boundary and then propagates inward; disk radius contracts from $R_o = 1.5$ mm to $R_1 \simeq 0.55$ mm.

sification at the middle cross section of the disk by plotting the ratio J_{d0}/J_d in the plane (R, τ) , with $R = r + u$ the current radial position. It is noted that, when $\tau \equiv \tau_\beta = 20$ s and contraction is fully developed, a narrow red strip of densification appears at the periphery; then, it propagates towards the interior until the whole cross section is more dense. The representation in the current domain determines the peculiar “boot” shape of the profile: as time goes on, the disk contracts and its radius contracts from $R_o = 1.5$ mm to $R_1 \simeq 0.55$ mm. On the other hand, stress analysis in the active disk can be relevant, as overall stress distribution might drive mechanical instability, which leads to a variety of different shapes at the end of the contraction [5,20,33,34]. The analysis of instabilities is beyond the scope of the present work, and it will mark our future efforts. However, through the aforementioned studies, we might have interesting clues about shape transitions by investigating the effects of AR on the evolution of radial stress σ_r and the hoop one σ_θ in the disk, which may drive further experiments.

We only report results for the case of constant radius. We compare the stress state in a thick ($AR \simeq 20$) and a thin ($AR \simeq 45$) disk. Panels (a) and (b) of Fig. 12 show the existence of two stress patterns: in a core region (beige), the stress is constant along the radius and spherical, that is, $\sigma_r = \sigma_\theta$; in the periphery (cyan), the stress varies with the radius and $\sigma_r \neq \sigma_\theta$. As the bulk contraction β is homogeneous and isotropic in the whole disk, these two regions are determined by the dynamics of liquid transport. In particular, the width of the peripheral region is of the order of the thickness because the solvent in this region can escape from both the lateral boundary and the top and bottom surfaces. In contrast, for the solvent in the core, the shortest path to exit the gel disk is through the top and bottom surfaces. Corresponding to our values of AR, we have $H_{\text{thin}} \simeq 0.04R_d$ and $H_{\text{thick}} = 0.1R_d$.

In particular, in Fig. 12, for $AR = 20$ we have essentially $\sigma_r < 0$ along all the radius, and σ_θ varying from negative to positive [see panel (a)]; for $AR = 45$ we have $\sigma_r > 0$ along all the radius, and σ_θ varying from positive to negative [see panel (b)]. The stress distribution for these two cases is typical of that found in frustrated domelike or saddelike disks [see Fig. (12), panels (c) and (d)] [20,33,34].

That is a preliminary requirement for observing instability patterns that can deliver domes or saddles, depending on other key factors, which are not investigated in the present paper.

E. Evolution of the aspect ratio during contraction

Finally, the geometry of the gel body suggests that we investigate the possibility of having dissipations η_r and η_θ in the plane, different from the vertical dissipation η_z . Dissipations are related to the resistances of the mesh to reorganize, which can be expected to be different. Our conjecture needs to be validated, and the analysis may stimulate further experiments in this direction.

As noted at the end of Sec. II, the system is controlled by the pair (μ_e, β) , and here we also analyze the combined effects of varying the chemical potential μ_e and active force β (scenario b).

We always consider a homogeneous and isotropic generalized force β . Nevertheless, during gel contraction, the radial

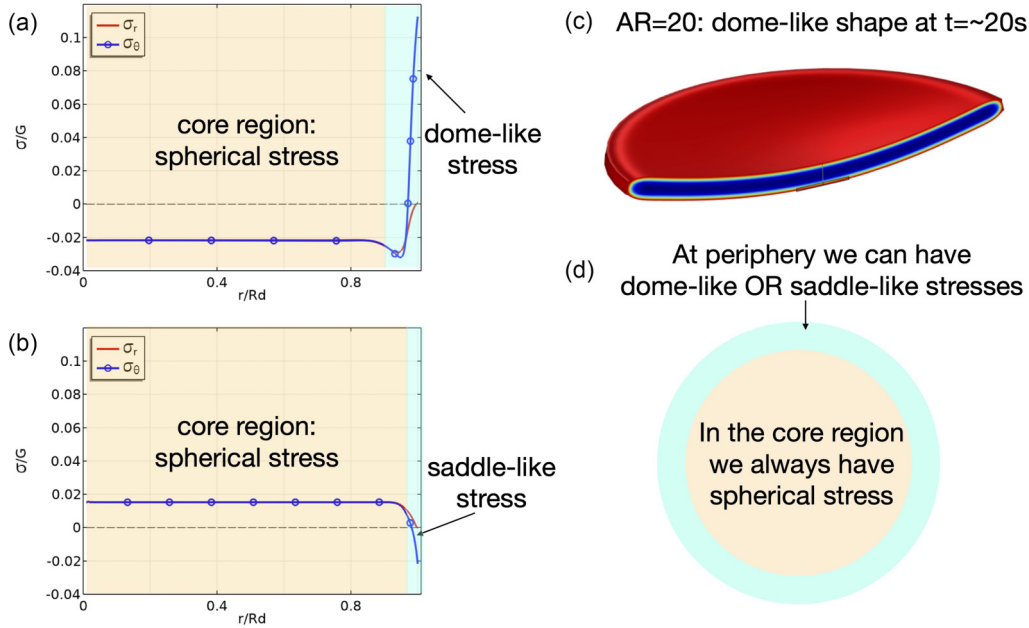


FIG. 12. Effect of AR on stress distribution for disks with constant radius. Panels (a) and (b) show the radial σ_r (red) and hoop σ_θ (blue) overall stresses vs the nondimensional radius r/R_d at $\tau = 20$ s, for AR = 20 and 45. (a) AR = 20: the hoop stress is negative in the core (beige) and positive at the periphery (cyan), a typical pattern of frustrated domelike shape.

829 and vertical stretches might differ locally, and each one of
 830 them can vary in time and space. We use the average values
 831 $R(\tau)$ and $H(\tau)$ of radius and thickness to describe the change
 832 in the aspect ratio of the disk, with $R(\tau)$ defined by Eq. (43)
 833 and $H(\tau)$ defined as $H(\tau) = \Lambda_z(\tau) H_d$ with

$$\Lambda_z(\tau) = 1 + \frac{1}{R_d} \int_0^{R_d} \frac{w(r, H_d, \tau)}{H_d} dr. \quad (46)$$

834 At any time τ , the ratio $H(\tau)/H_o$ can be plotted against the
 835 ratio $R(\tau)/R_o$ to illustrate the evolution path of the radial and
 836 vertical stretches, that is, the curve $\tau \mapsto (R(\tau)/R_o, H(\tau)/H_o)$,
 837 plotted in the plane $(R/R_o, H/H_o)$. In Fig. 13, the curve has
 838 been represented for a disk with AR = 22 and $R_o = 1.5$ mm.
 839 In that plot, the dashed line represents an isotropic evolution,
 840 during which the aspect ratio remains constant during network
 841 contraction.

842 For each of the two analyzed cases, corresponding to
 843 scenario (a) (red) and (b) (blue), we show two curves,
 844 one corresponding to equal dissipations (diamond markers), $\eta_r =$
 845 $\eta_\theta = \eta_z$, and the other with different horizontal and vertical
 846 dissipations (asterisk markers), $\eta_r = \eta_\theta = 2 \eta_z$. We note that
 847 the evolution is very sensitive to dissipation, while the dif-
 848 ferences between scenarios (a) and (b) are less noticeable.
 849 For all simulations, the system evolves via a characteristic
 850 path. It departs from the isotropic contraction path, but in
 851 the case with equal dissipations the steady-state configuration
 852 ends on the dashed line (i.e., on the isotropic path), while
 853 the case with different dissipations ends far from it. In par-
 854 ticular, when $\eta_r = \eta_z$, the contraction is almost isotropic until
 855 $H/H_o = R/R_o \sim 0.8$; then, the radial contraction is faster,
 856 and eventually the vertical one becomes faster. When $\eta_r = 2 \eta_z$,
 857 the vertical contraction is much faster than the radial one, and
 858 the final state is not isotropic.

These first clues deserve to be investigated further both ex- 859
 860 perimentally and numerically to stress the morphing chances
 861 of active gel.

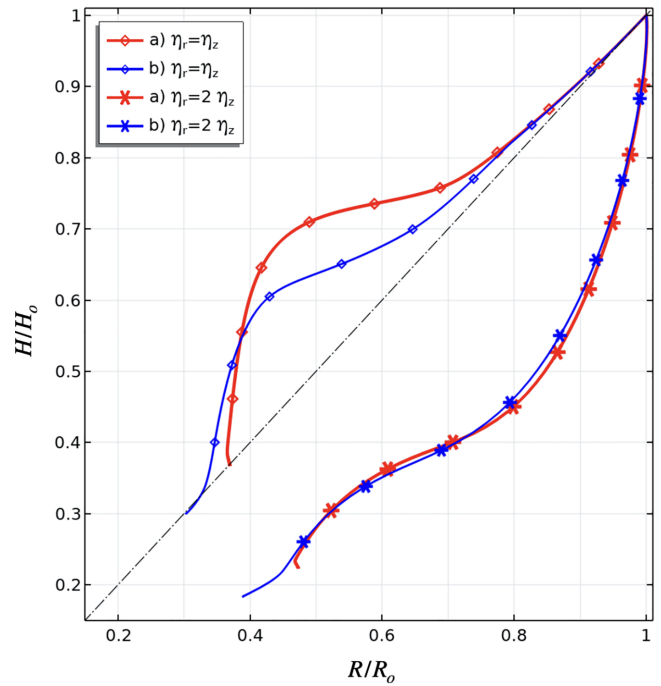


FIG. 13. Thickness ratio H/H_o vs radius ratio R/R_o during contraction for cases (a) (red) and (b) (blue) with equal friction $\eta_r = \eta_z$ (diamond) and differential friction $\eta_r = 2 \eta_z$ (star); $\eta_r = 10^5$ Pa s. The dashed line represents isotropic contractions; with different frictions, the radial and vertical contractions are not isotropic. Disk geometry: $R_o = 1.5$ mm, AR = 22.

VI. CONCLUSIONS AND FUTURE DIRECTIONS

We discussed the interplay between elasticity, liquid transport, and self-contractions in active gel disks from the perspective of continuum mechanics. The transient problem for gel disks of different aspect ratios has been solved, and different aspects of the problem have been discussed: the regimes of fast and slow liquid transport, the characteristic times of the contraction and liquid transport dynamics, and the changes in the stress state in gel disks of different thickness. In doing so, the analysis of the competitive role of gel contractility and liquid flow in driving the mechanics of the active gel has been exploited.

To keep the model easy, the numerical model has been developed under the hypothesis of cylindrical symmetry, which excludes the challenge to observe disk morphings, which are not compatible with the cylindrical symmetry. Actually, we are planning to give up the symmetry hypothesis above and investigate the blossom of stresses in the disk, which may drive instability patterns and, consequently, a variety of steady shapes of the gel. This was beyond the scope of the present work, and it will mark our future efforts.

Giving up the symmetry hypothesis also makes more interesting the identification of the determinants of possible changes in shape, whose control would make it possible to get actuators based on self-contractile gels, a promising field that can be set within the framework here presented.

ACKNOWLEDGMENTS

This work has been supported by MAECI (Ministry of Foreign Affairs and International Cooperation) and MOST

(Ministry of Science and Technology–State of Israel) through the project PAMM. A.B.-G. is also grateful to the Israel Science Foundation (Grant No. 2101/20). G.L. is grateful to the MOST for the Jabotinsky PhD Scholarship. F.R. also thanks INDAM-GNFM for support with Progetti Giovani GNFM 2020. L.T. acknowledges the Italian grant PRIN 2017KL4EF3, “Mathematics of active materials: From mechanobiology to smart devices.”

APPENDIX

1. Details of finite-element analysis

Equations (15), (16), and (22), together with the boundary (26) and initial (27) conditions, are rewritten in a weak form and implemented in the software COMSOL MULTIPHYSICS by using the Weak-Form physics interface. The calculus domain is the rectangular domain S_d , which is meshed with triangular elements whose maximum mesh size is $H_d/10$, yielding about 200 K DOFs. Lagrangian polynomials are used as shape functions: polynomials of order 4 for the displacement and the solvent concentration, of order 3 for the volumetric constraint, of order 2 for the boundary conditions (also implemented in weak form), and of order 1 for the remodeling variables. The whole set of coupled equations are solved by using the Newton method with variable damping as the nonlinear solver; the linear solver is the direct solver Pardiso, while the time-dependent solver uses the BDF method with order 1–2. The time-dependent analysis starts at the initial state \mathcal{B}_0 and stops at a final equilibrium state \mathcal{B}_1 , which is preselected.

-
- [1] P. M. Bendix, G. H. Koenderink, D. Cuvelier, Z. Dogic, B. N. Koeleman, W. M. Briehar, C. M. Field, L. Mahadevan, and D. A. Weitz, A quantitative analysis of contractility in active cytoskeletal protein networks, *Biophys. J.* **94**, 3126 (2008).
 - [2] G. H. Koenderink, Z. Dogic, F. Nakamura, P. M. Bendix, F. C. MacKintosh, J. H. Hartwig, T. P. Stossel, and D. A. Weitz, An active biopolymer network controlled by molecular motors, *Proc. Natl. Acad. Sci. USA* **106**, 15192 (2009).
 - [3] M. K. Matthias Schuppler, F. C. Keber, and A. R. Bausch, Boundaries steer the contraction of active gels, *Nat. Commun.* **7**, 13120 (2016).
 - [4] A. Bernheim-Groswasser, N. S. Gov, S. A. Safran, and S. Tzlil, Living matter: Mesoscopic active materials, *Adv. Mater.* **30**, 1707028 (2018).
 - [5] Y. Ideses, V. Erukhimovitch, R. Brand, D. Jourdain, J. Salmeron Hernandez, U. R. Gabinet, S. A. Safran, K. Kruse, and A. Bernheim-Groswasser, Spontaneous buckling of contractile poroelastic actomyosin sheets, *Nat. Commun.* **9**, 2461 (2018).
 - [6] F. Backouche, L. Haviv, D. Groswasser, and A. Bernheim-Groswasser, Active gels: Dynamics of patterning and self-organization, *Phys. Biol.* **3**, 264 (2006).
 - [7] Y. Ideses, A. Sonn-Segev, Y. Roichman, and A. Bernheim-Groswasser, Myosin II does it all: Assembly, remodeling, and disassembly of actin networks are governed by Myosin II activity, *Soft Matter* **9**, 7127 (2013).
 - [8] M. C. Marchetti, J. F. Joanny, S. Ramaswamy, T. B. Liverpool, J. Prost, M. Rao, and R. A. Simha, Hydrodynamics of soft active matter, *Rev. Mod. Phys.* **85**, 1143 (2013).
 - [9] J. Prost, F. Jülicher, and J.-F. Joanny, Active gel physics, *Nat. Phys.* **11**, 111 (2015).
 - [10] F. C. MacKintosh and A. J. Levine, Nonequilibrium mechanics and dynamics of motor-activated gels, *Phys. Rev. Lett.* **100**, 018104 (2008).
 - [11] S. Banerjee and M. C. Marchetti, Instabilities and oscillations in isotropic active gels, *Soft Matter* **7**, 463 (2011).
 - [12] P. Ronceray, C. P. Broedersz, and M. Lenz, Fiber networks amplify active stress, *Proc. Natl. Acad. Sci. USA* **113**, 2827 (2016).
 - [13] M. Bacca, O. A. Saleh, and R. M. McMeeking, Contraction of polymer gels created by the activity of molecular motors, *Soft Matter* **15**, 4467 (2019).
 - [14] M. Curatolo, P. Nardinocchi, and L. Teresi, Dynamics of active swelling in contractile polymer gels, *J. Mech. Phys. Solids* **135**, 103807 (2020).
 - [15] M. Curatolo, P. Nardinocchi, and L. Teresi, Mechanics of active gel spheres under bulk contraction, *Int. J. Mech. Sci.* **193**, 106147 (2021).
 - [16] W. Hong, X. Zhao, J. Zhou, and Z. Suo, A theory of coupled diffusion and large deformation in polymeric gels, *J. Mech. Phys. Solids* **56**, 1779 (2008).

- [17] S. A. Chester and L. Anand, A coupled theory of fluid permeation and large deformations for elastomeric materials, *J. Mech. Phys. Solids* **58**, 1879 (2010).
- [18] A. Lucantonio, P. Nardinocchi, and L. Teresi, Transient analysis of swelling-induced large deformations in polymer gels, *J. Mech. Phys. Solids* **61**, 205 (2013).
- [19] P. Nardinocchi, L. Teresi, and V. Varano, The elastic metric: A review of elasticity with large distortions, *Int. J. Non Lin. Mech.* **56**, 34 (2013).
- [20] E. Sharon and E. Efrati, The mechanics of non-Euclidean plates, *Soft Matter* **6**, 5693 (2010).
- [21] D. A. Matoz-Fernandez, F. A. Davidson, N. R. Stanley-Wall, and R. Sknepnek, Wrinkle patterns in active viscoelastic thin sheets, *Phys. Rev. Res.* **2**, 013165 (2020).
- [22] M. Doi, Gel dynamics, *J. Phys. Soc. Jpn.* **78**, 052001 (2009).
- [23] M. Fujine, T. Takigawa, and K. Urayama, Strain-driven swelling and accompanying stress reduction in polymer gels under biaxial stretching, *Macromolecules* **48**, 3622 (2015).
- [24] M. Curatolo, P. Nardinocchi, and L. Teresi, Driving water cavitation in a hydrogel cavity, *Soft Matter* **14**, 2310 (2018).
- [25] P. J. Flory and J. Rehner, Jr., Statistical mechanics of cross-linked polymer networks I. Rubberlike elasticity, *J. Chem. Phys.* **11**, 512 (1943).
- [26] P. J. Flory and J. Rehner, Statistical mechanics of cross-linked polymer networks II. Swelling, *J. Chem. Phys.* **11**, 521 (1943).
- [27] M. Gurtin, E. Fried, and L. Anand, *The Mechanics and Thermodynamics of Continua* (Cambridge University Press, Cambridge, 2010).
- [28] L. Teresi, M. Curatolo, and P. Nardinocchi, Active gel: A continuum physics perspective, in *Modeling of Mass Transport Processes in Biological Media*, edited by S. Becker, A. V. Kuznetsov, F. de Monte, G. Pontrelli, and D. Zhao (Academic Press, 2022), Chap. 9, pp. 287–309.
- [29] D. S. Ebert, F. K. Musgrave, D. Peachey, K. Perlin, and S. Worley, *Texturing and Modeling: A Procedural Approach*, 3rd ed. (Kaufmann, San Francisco, 2002).
- [30] We used the first-order smooth step function: it is the improved version of the commonly used first-order smooth step function, equivalent to the second order of its general form, with zero first- and second-order derivatives at τ_0 and τ_1 , which can be easily implemented numerically. In particular, the ramp in the interval (τ_0, τ_1) for the function $\mu_e(\tau)$ is given by $6(\tau/\tau_\mu)^5 - 15(\tau/\tau_\mu)^4 + 10(\tau/\tau_\mu)^3$.
- [31] L. Haviv, D. Gillo, F. Backouche, and A. Bernheim-Groswasser, A cytoskeletal demolition worker: Myosin II acts as an actin depolymerization agent, *J. Mol. Biol.* **375**, 325 (2008).
- [32] About the bottom curve and the jump, it is due to the onset of an out-of-plane instability that temporarily decreases the radial velocity.
- [33] E. Efrati, E. Sharon, and R. Kupferman, Buckling transition and boundary layer in non-Euclidean plates, *Phys. Rev. E* **80**, 016602 (2009).
- [34] M. Pezzulla, S. A. Shillig, P. Nardinocchi, and D. P. Holmes, Morphing of geometric composites via residual swelling, *Soft Matter* **11**, 5812 (2015).